

Population in Galaxies and X-ray Luminosity Function

The Cartwheel galaxy as a stepping stone for binaries formation

Anna Wolter¹, Guido Consolandi^{1,2}, Marcella Longhetti¹,
Marco Landoni¹ and Andrea Bianco¹

¹INAF-Osservatorio Astronomico di Brera,
Via Brera 28, I-20121 Milano, Italy
email: anna.wolter@inaf.it

²Università degli Studi di Milano Bicocca,
Piazza dell'Ateneo Nuovo, 1, I-20126 Milano, Italy
email: guido.consolandi@inaf.it

Abstract. Ultraluminous X-ray sources (ULXs) are end points of stellar evolution. They are mostly interpreted as binary systems with a massive donor. They are also the most probable progenitors for BH-BH, and even more, for BH-NS coalescence. Parameters of ULXs are not known and need to be better determined, in particular the link with the metallicity of the environment which has been invoked frequently but not proven strongly. We have tackled this problem by using a MUSE DEEP mosaic of the Cartwheel galaxy and applying a Monte Carlo code that jointly fits spectroscopy and photometry. We measure the metallicity of the emitting gas in the ring and at the positions of X-ray sources by constructing spatially resolved emission line ratio maps and BPT diagnostic maps. The Cartwheel is the archetypal ring galaxy and the location and formation time of new stellar populations is easier to reconstruct than in more normal galaxies. It has the largest population of ULXs ever observed in a single galaxy (16 sources have been classified as ULXs in Chandra and XMM-Newton data). The Cartwheel galaxy is therefore the ideal laboratory to study the relation between Star Formation (SF Rates and SF History) and number of ULXs and also their final fate. We find that the age of the stellar population in the outer ring is consistent with being produced in the impact ($\leq 300 Myr$) and that the metallicity is mostly sub-solar, even if solutions can be found with a solar metallicity that account for most observed properties. The findings for the Cartwheel will be a testbed for further modelisation of binary formation and evolution paths.

Keywords. stars: binaries, galaxies: individual (Cartwheel), galaxies: peculiar, galaxies: interaction, galaxies: evolution

1. Introduction

Why did we choose the Cartwheel galaxy? The Cartwheel is the epitome of the Ring Galaxies (RiGs), in which many ultra luminous X-ray sources (ULXs) are produced as end points of stellar evolution. We have shown (see later) that ULXs are in general the high luminosity tail of high mass X-ray binaries (HMXB; see also contributions by Roberts or Kowlakas, this volume). They are the testimony of a recent event: the gravitational encounter of two galaxies. In RiGs, the location and formation time of new stellar populations are easier to reconstruct than in normal spirals due to the simpler geometry and dynamics. Brighter ULXs seem to be preferentially found in low metallicity environments. Two possibilities have been put forward: a) the largest black holes (BH) are constructed from direct collapse of low metallicity stars (e.g. [Mapelli *et al.* 2009](#))

or b) metal-poor X-ray binaries are more luminous than their metal-rich peers (Linden *et al.* 2010, which could be the case for both BH or neutron stars (NS) counterparts (see also contributions by Artale, this volume).

The Cartwheel belongs to a compact group of 4 members (Iovino 2002) at a distance of $D = 122$ Mpc. The shock wave of the encounter with one of the group galaxies has launched a shock wave that has triggered star formation and enhanced emission in all bands. The consequence of this star formation is the large number of ULXs found, especially in the ring - see Wolter *et al.* (2015).

The recent Gravitational Waves (GW) detections have increased the interest of ULXs as possible sites of coalescence. Many authors have used the ULXs as progenitors to compute the expectancy for GW detection of different kinds of merging, in particular the NS-BH event which has not been detected yet. Many recent estimates of expected rates (e.g. Inoue *et al.* 2016) do take into consideration the ULX properties (Luminosity Function, active time, frequency by galaxy mass or SFR). However, many of these parameters are very uncertain or not known (see also contributions by Giacobbo *et al.*, by Erkut *et al.* and by Fabrika *et al.* this volume).

We use an operative definition of ULX as an extra-galactic, point-like, non-nuclear, X-ray source with $10^{39} \text{ erg/s} < L_X < 10^{42} \text{ erg/s}$ (Fabbiano 1989). This definition is bound to create a mixed class of sources and includes interlopers, like background AGNs, and at least a subclass of Supernovae, possibly numbering about 25% of all ULXs (Swartz *et al.* 2011). The majority of ULXs nevertheless are thought to be binary systems, with a degenerate object and a large (in most cases) companion. The engine of the system might be: a) an Intermediate Mass BH ($10^{2-5} M_{\odot}$ - this was the initial guess but now runs a bit out of fashion; b) a BH with a heavy stellar mass (30-100 M_{\odot}) or c) a Neutron Star - this has been proven for at least 5 cases (Bachetti *et al.* 2014, Israel *et al.* 2017a,b, Fuerst *et al.* 2016, Carpano *et al.* 2018) out of a few hundred ULXs.

2. The X-ray Luminosity Function of ULXs

First we use the X-ray luminosity function (XLF) to show that ULXs are related to HMXB, which are the subject of this meeting, and therefore deserve attention here. A number of authors, including us, has produced the XLF for individual galaxies with a large number of ULXs (Cartwheel: Wolter & Trinchieri 2004; Antennae: Zezas *et al.* 2007; NGC337: Somers *et al.* 2013; NGC 2276: Wolter *et al.* 2015) and compared it with the so-called universal luminosity function of HMXB by Grimm *et al.* (2003). The normalization of the XLF for the Star Formation Rate (SFR), measured typically via the $H\alpha$ luminosity, is consistent with the idea that ULXs are linked to recent star formation bursts. The smooth connection with the lower luminosity sources and the slope of the XLF are consistent with our hypothesis.

This is also shown by the XLF of both a large number of ULXs collected in the rings of seven collisional RiGs (Wolter *et al.* 2018) and those in the collection of nearby galaxies (Swartz *et al.* 2011) observed by Chandra, which yield a similar number of ULXs and consistent results between each other, even if the RiGs have a possible excess at high luminosity. The combination of many galaxies relies on the assumption that we are witnessing a single burst of star formation in each galaxy, with a reasonable short age (possibly less than 100 Myr as per the simulations of Renaud *et al.* 2018), close to the formation time of HMXB, and that the spread in metallicity is not large. In any case, the effect of metallicity is not predominant with respect to the SFR (see e.g. Mapelli *et al.* 2010).

The Cartwheel, with its 15 out of 65 sources in the collection of ring galaxies, is the best testbed in which to search for new information about the environment of formation and evolution of ULXs and HMXB in general. A measure of the metallicity of the Cartwheel is available in the literature (Fosbury *et al.* 1977), measured in the brightest HII regions. The



Figure 1. Three color image derived from MUSE data - using filters matching as close as possible the g, i and r Gunn filters.

age of the star burst is not known, even if a few estimates of the epoch of the encounter are available in the literature: Higdon (Higdon 1996) estimates 300 Myr from the impact from the HI velocity field; Amram (Amram *et al.* 1998) estimate the age of the ring at > 200 Myr from $H\alpha$ kinematics (13-30 km/s expansion); while Renaud (Renaud *et al.* 2018) run detailed simulations that imply an age < 100 Myr for the persistence of ring.

We intend therefore to study the Cartwheel to address these issues.

3. MUSE data

The Cartwheel was observed by MUSE in Aug 2014 for calibration purposes with a mosaic of four 4 ksec pointings to include the entire ring (1.4×1.5 arcmin). The data have been downloaded from the ESO archive. The MUSE 3D science data cubes have their instrumental signature removed, and are astrometrically calibrated, sky-subtracted, wavelength and flux calibrated, using the MUSE pipeline, version muse-1.4 and higher. We show in Figure 1 a color image, obtained by filtering on the Gunn filters g, i, and r the band pass of MUSE (details in Wolter *et al.* in prep).

To robustly estimate emission line fluxes, we accounted for the stellar absorptions underlying the Balmer emission lines that fall in the MUSE spectral window: $H\alpha$ and $H\beta$. For this, we used the code GANDALF (Sarzi *et al.* 2006) complemented by the penalize pixel-fitting code (Cappellari & Emsellem 2004) to simultaneously model the stellar continuum and the emission lines in individual spaxels with $S/N > 5$. The stellar continuum was modeled with the superposition of stellar templates from the MILES library (Vazdekis *et al.* 2010) convolved by the stellar line-of-sight velocity distribution, whereas the emission lines and kinematics were modeled assuming a Gaussian profile. In each spaxel, the modeled stellar continuum spectrum was subtracted from the observed spectrum to obtain a final datacube of pure emission lines that is free of stellar absorption.

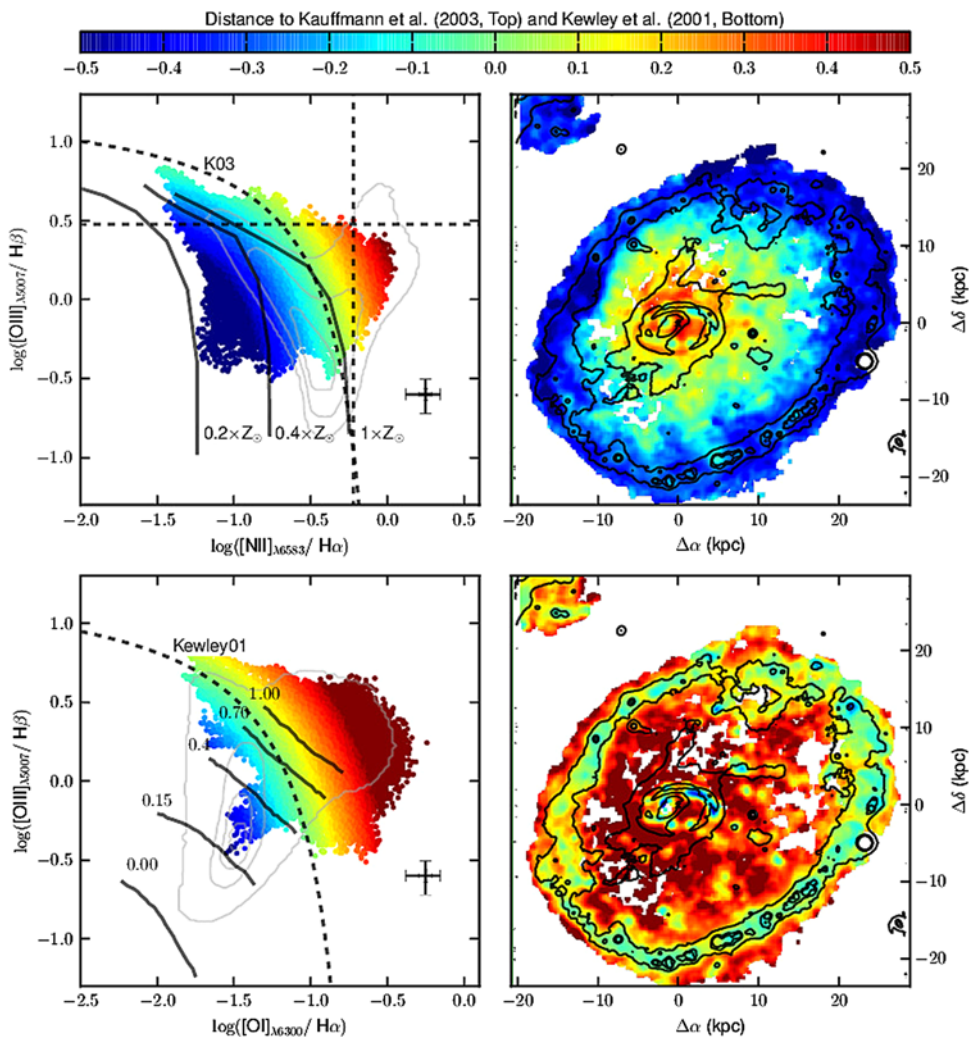


Figure 2. BTP diagrams: see text for details. *Top-left:* $[\text{OIII}]\lambda 5007/\text{H}\beta$ vs. $[\text{NII}]\lambda 6583/\text{H}\alpha$. *Top-right:* map of the spaxel contributing to the BPT, color-coded as in the top-left panel. *Bottom-left:* $[\text{OIII}]\lambda 5007/\text{H}\beta$ vs. $[\text{OI}]\lambda 6300/\text{H}\alpha$. *Bottom-right:* map of the spaxels contributing to the BPT, color-coded as in the bottom-left panel.

3.1. Metallicity

We have extracted “line” images (for $\text{H}\alpha$, $\text{H}\beta$, $[\text{OIII}]$, $[\text{OI}]$ and $[\text{NII}]$). We can then use those images to compute standard classification diagrams resolved in spaxels, as the two BTP diagnostic maps shown in Figure 2. In the top-left panel the $[\text{OIII}]\lambda 5007/\text{H}\beta$ vs. $[\text{NII}]\lambda 6583/\text{H}\alpha$ is plotted. The dashed curve separates AGN from HII regions and is adopted from [Kauffmann *et al.* 2003](#) (Ka03). Data (in the top-right panel) are color-coded according to their minimum distance to the Ka03 curve. The black crosses indicate the typical error of the ratio of lines with a $\text{S/N} \sim 15/5$. Thick solid lines show the three different photoionization models at different metallicities ($0.2 Z_{\odot}$, $0.4 Z_{\odot}$ and Z_{\odot}) by [Kewley *et al.* \(2001\)](#).

In the bottom-left panel the $[\text{OIII}]\lambda 5007/\text{H}\beta$ vs. $[\text{OI}]\lambda 6300/\text{H}\alpha$ is plotted. The dashed curve separates AGN from HII regions and is adopted from [Kewley *et al.* 2001](#) (Ke01).

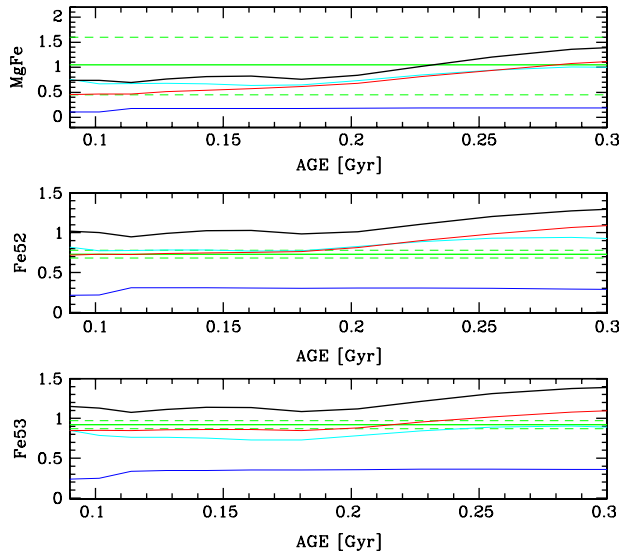


Figure 3. Comparison between BC03 models expectations and MgFe (*top panel*), Fe5270 (*middle panel*) and Fe5335 (*lower panel*) indices measures of the Cartwheel outer ring spectrum. The green lines represent our measures (*solid line*) and their errors (*short dashed line*). In each panel, expected indices values as a function of the age of a SSP are reported for solar metallicity (*black line*), $Z = 0.4 Z_{\odot}$ (*red line*), $Z = 0.2 Z_{\odot}$ (*cyan line*) and $Z = 0.02 Z_{\odot}$ (*blue line*).

Data (in the bottom-right panel) are color-coded according to their minimum distance to the Ke01 curve. The black crosses indicate the typical error of the ratio of lines with a S/N $\sim 15/5$. Thick solid lines show the five different shock models by Rich *et al.* 2011, indicating five different fractions (from 0 to 1) of H α flux contributed by shocks.

A general assessment of the metallicity in the galaxy shows that the metallicity of the ring is consistently lower than in the rest of the galaxy. The small portion of G1 visible in the upper left corner shows about the same metallicity of the ring. The central region appears supersolar. However, as shown in the bottom panels, where [OI] is used instead of [NII], we cannot exclude the presence of shocks that contribute to the line ratios.

3.2. Spectra and inferences

It is notorious that metallicity of stars and age of the galaxy give similar effects on the optical spectra. Nevertheless we try to measure them separately by looking at some Lick narrowband spectral indices like those related to the Mg and Fe absorption features in the range 5300-5500 Å (i.e., Mgb, Fe5270, F5335, MgFe). We compare our measures with the expectations of Bruzual & Charlot 2003 (BC03) models (Simple Stellar Population SSP, Chabrier IMF) for different metallicities (i.e., $Z = Z_{\odot}$; $Z = 0.4 Z_{\odot}$; $Z = 0.2 Z_{\odot}$; $Z = 0.02 Z_{\odot}$), as shown in Fig. 3.

The star metallicity is consistent with being 20-40% solar, in particular, especially from the iron indices Fe5335 and Fe5270 (for which our measures result to have a better accuracy), it is $Z = 0.4 \times$ solar if the age of the star population is 200 Myr, while it is $0.2 \times$ solar if the age is 300 Myr. This would confirm the picture in which the age is small (less than 400 Myr) and, even if the correlation between age and metallicity is still present, we can constrain the interval between 20-40% solar, consistent with the majority

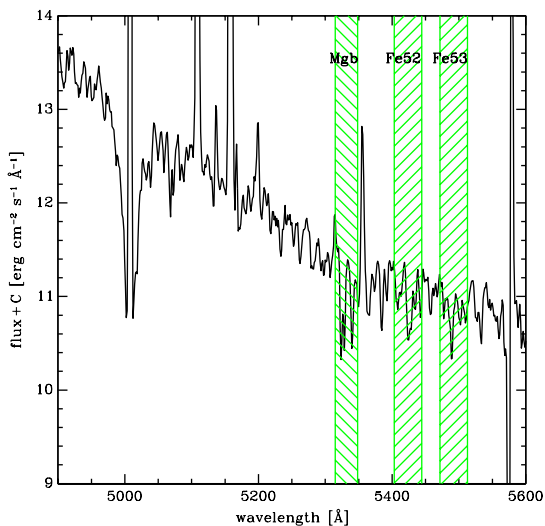


Figure 4. Cartwheel MUSE outer ring spectrum. The green dashed bands mark the spectral regions involved in the metallicity Lick indices which have been estimated in this work.

of the star having been produced in the impact, with a less than solar gas, possibly mixed between the original gas of the Cartwheel and the surrounding environment.

4. Spectro-photometric fitting with MultiNest

Is the timing right? Can we measure the age of the population? Given the age and metallicity correlation, can we disentangle them?

These are amongst the questions we would like to address with the MUSE data, in combination with all other multi-wavelength measures. To this aim, we have adapted the code by Fossati & Mendel (see Fossati *et al.* 2018 on the VESTIGE survey) which exploits a *MULTINEST* fit. It applies a Monte-Carlo Spectro-Photometric Fitter which derives the star formation history (SFH) by fitting high resolution (Bruzual&Charlot) population models. A linear interpolation of the stellar models (where Q_{age} is the look-back time of the event and T_q is the characteristic time scale) is performed, and the result is scaled in luminosity as part of the fitting procedure. The procedure includes nebular emission lines (ionizing radiation absorbed by gas) and dust attenuation.

We collect all the available photometric information in the UV-O-IR band. We select three different spatial regions: the outer ring, the middle zone and the inner (and nuclear) ring. We focus here on the outer ring, in which the majority of the stars should be produced in the impact, and which has a higher brightness, which helps in reducing degrees of freedom to the fitted models. The inner ring has a mix of old and new population which is quite more complicated to simulate with a simple star formation history. The middle zone is fainter a therefore more uncertain, even if very interesting from the point of view of confirming simulations.

We derive photometric points for the outer ring, and extract a MUSE spectrum from the same spatial region, as input to the spectrophotometric fitter. We plot the results for the solar value and for 20% solar - which are the extremes we considered - in Figure 5, where in the bottom left panel: blue indicates the young component, with stellar emission and nebular lines, while red represents the old component (> 10 Myr). The shape of the SFH is a single burst, exponentially quenched. The fitted parameters are the age of the burst ($Q_{age} = 300/132$ Myr) and the quenching scale ($T_q = 69/19$ Myr) for metallicity $Z = Z_{\odot}$ (top) and $0.2 Z_{\odot}$ (bottom) respectively.

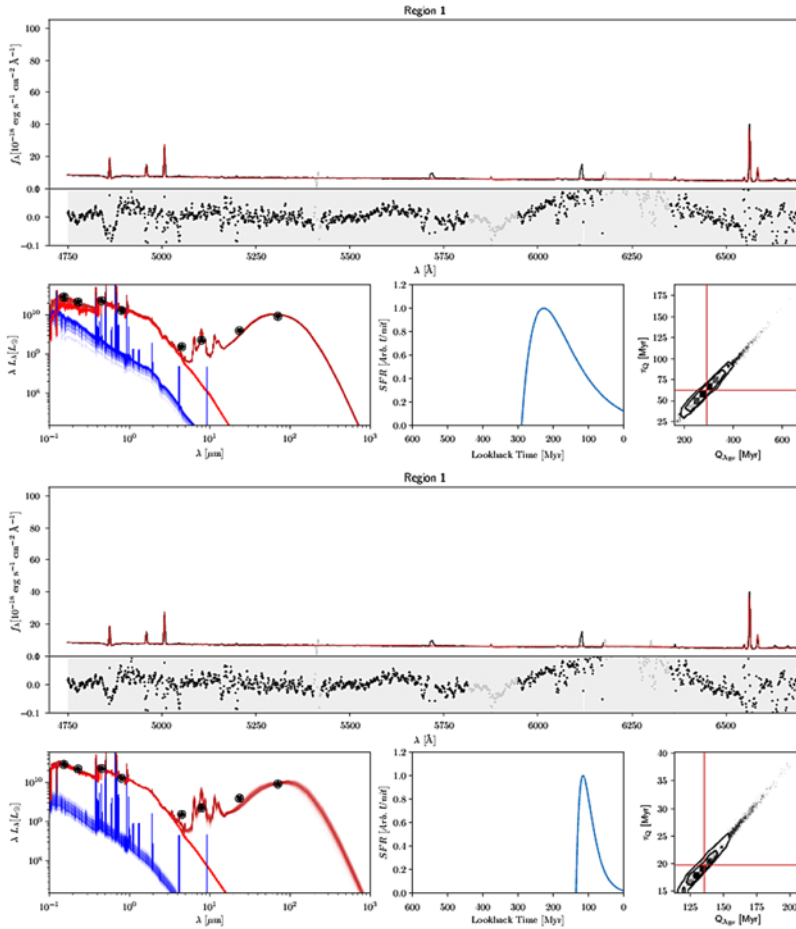


Figure 5. a) *Top figure:* solar metallicity; b) *Bottom figure:* 20% solar metallicity. Both figures are thus structured: *Top:* Results of the MC-SPF fitting for the outer ring. Upper panel: MUSE spectrum (black) and best fit model (dark red). Regions where the spectrum is plotted in grey are not used in the fit. The fit residuals ($Data - Model$) are shown below the spectrum and the grey shaded area shows the 1σ uncertainties. *Lower left panel:* photometric data points in black. The blue line represents the stellar emission with nebular lines from the young component (Age < 10 Myr), the red lines are from the old component (Age > 10 Myr), while the dark red lines are the total model including the dust emission. *Lower middle panel:* reconstructed SFH from the fitting procedure. *Lower right panel:* marginalised likelihood maps for the Q_{age} and T_q fit parameters. The red lines show the median value for each parameter, while the black contours show the 13σ confidence intervals

5. X-ray band information

One of our aims is to compare the environment properties with the production of ULXs to gather information on the formation mechanism. The first step is to compare the X-ray emission observed by Chandra to the optical one measured by MUSE, as shown in Figure 6. In the same figure, red circles indicate the background objects, easily traceable in the MUSE data cube. No particularly X-ray bright interloper is found in the ring region.

First we investigate if the metallicity is different at the ULXs positions from the rest of the ring. We compute the metallicity by following the prescription of Curti *et al.* 2017,

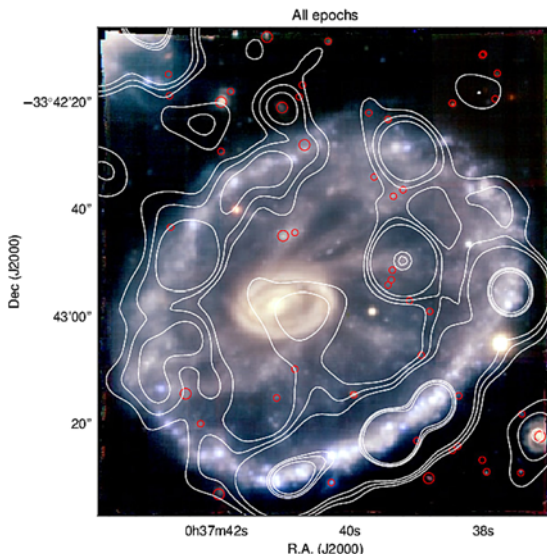


Figure 6. The RGB MUSE image reports the position of the background sources (red circles). The X-ray emission from the Chandra observation (Wolter & Trinchieri 2004) is superposed in white contours.

which calibrate the relation differently for different metallicity ranges, by using the O_3N_2 index defined as: $O_3N_2 = ([OIII]\lambda 5007/H\beta)/([NII]\lambda 6584/H\alpha)$.

We extract the metallicity value at the position of the HII regions listed in (Higdon 1995), and at the ULXs positions from (Wolter & Trinchieri 2004). The range of metallicities - $12 + \log(O/H) = 8.16 - 8.47$ - is the same for the two samples, indicating that a) a range of values is found even in the ring; b) the ULXs do not occupy a privileged position with respect to the metallicity distribution (see also the contribution by Kouroumpatzakis *et al.*, this volume).

6. Conclusion

ULXs are in the majority binaries, whether NS or BH, produced by a recent episode of Star Formation. The recent construction of XLF for RiGs suggests the presence of a larger number of high luminosity sources in collisional environments. This results may be applicable to constrain estimates for GW events. Galaxies like the Cartwheel represent sizable samples of ULXs and are therefore the most interesting to study. We have exploited the MUSE dataset that allows us to derive spatially resolved information to compare with multi-wavelength data. We find that metallicity is 20-40% solar in the external ring, consistently in both stars and gas, but we cannot exclude yet from our spectrophotometric fitting procedure that the metallicity is solar. From the above results it follows that the age of the stellar population produced in the encounter is ≤ 300 Myr and possibly smaller, consistent with the timing of HMXB formation, which reinforces the interpretation of ULX system as the high luminosity (higher mass transfer? higher magnetic field?) tail of HMXB. ULXs are not found in special regions with respect to the rest of the galaxy, or at least of the ring, for what concerns metallicity. While this point needs to be further studied, it might lessen the importance of the environment for the formation of ULXs and strengthen the importance of the timing of the event.

In the future we plan to perform a detailed comparison with simulations (Renaud *et al.* 2018, Mapelli & Mayer 2012) for different regions of the galaxy; we will exploit available long-slit spectra for determining the ionization parameter and even better calibrate the

metallicity relations. These results will be applied then to constrain formation models of ULXs (e.g. Wiktorowicz *et al.* 2017).

References

- Amram, P., Mendes de Oliveira, C., Boulesteix, J. & Balkowski, C., 1998, *A&A*, 330, 881
- Bachetti, M. *et al.* 2014, *Nature*, 514, 202
- Bruzual, G., & Charlot, S., 2003, *MNRAS*, 344, 1000
- Cappellari, M., & Emsellem, E. 2004, *PASP*, 116, 138
- Carpano, S., Haberl, F., Maitra, C. & Vasilopoulos, G., 2018, *MNRAS*, 476L, 45
- Curti, M., Cresci, G., Mannucci, F., Marconi, A., Maiolino, R., & Esposito, S., *MNRAS*, 465, 1384
- Fabbiano, G., 1989, *ARA&A*, 27, 87
- Fosbury, R. A. E. & Hawarden, T. G., 1977, *MNRAS*, 178, 473
- Fossati, M., *et al.*, *A&A*, 2018, 614, 57
- Fürst, F., Walton, D. J., Stern, D., Bachetti, M., Barret, D., Brightman, M., Harrison, F. A. & Rana, V., 2016, *ApJ*, 834, 77
- Grimm, H.-J., Gilfanov, M. & Sunyaev, R., 2003, *MNRAS*, 339, 793
- Higdon, J. L., 1995, *ApJ*, 455, 524
- Higdon, J. L., 1996, *ApJ*, 467, 241
- Inoue, T., Tanaka, Y.T., & Isobe, N., 2016, *MNRAS*, 461, 4329
- Iovino, A., 2002, *AJ*, 124, 2471
- Israel, G. L. *et al.*, 2017a, *MNRAS*, 466L, 48
- Israel, G. L. *et al.*, 2017b, *Science*, 355, 817
- Kauffmann, G., Heckman, T.M., Tremonti, C., *et al.* 2003, *MNRAS*, 346, 1055
- Kewley, L.J., Dopita, M.A., Sutherland, R.S., Heisler, C.A., & Trevena, J. 2001, *ApJ*, 556, 121
- Linden, T., Kalogera, V., Sepinsky, J. F., Prestwich, A., Zezas, A. & Gallagher, J. S., 2010, *ApJ*, 725, 1984
- Mapelli, M., Colpi, M. & Zampieri, L., 2009, *MNRAS*, 395L, 71
- Mapelli, M., Ripamonti, E., Zampieri, L., Colpi, M. & Bressan, A., 2010, *MNRAS*, 408, 234
- Mapelli, M. & Mayer, L., *MNRAS*, 420, 1158
- Renaud, F. *et al.*, 2018, *MNRAS*, 473, 585
- Rich, J.A., Kewley, L.J., & Dopita, M.A. 2011, *ApJ*, 734, 87
- Sarzi, M., Falcón-Barroso, J., Davies, R. L., *et al.* 2006, *MNRAS*, 366, 1151
- Somers, G., Mathur, S., Martini, P., Watson, L., Grier, C.J. & Ferrarese, L., 2013, *ApJ*, 777, 7
- Swartz, D. A., Soria, R., Tennant, A. F. & Yukita, M. *ApJ*, 741, 49
- Vazdekis, A., Sánchez-Blázquez, P., Falcón-Barroso, J., *et al.* 2010, *MNRAS*, 404, 1639
- Wiktorowicz, G., Sobolewska, M., Lasota, J.-P. & Belczynski, K., 2017, *ApJ*, 846, 17
- Wolter, A. & Trinchieri, G, *A&A*, 426, 787
- Wolter, A., Esposito, P., Mapelli, M., Pizzolato, F. & Ripamonti, E., 2015, *MNRAS*, 448, 781
- Wolter, A., Fruscione, A. & Mapelli, M., 2018 *ApJ*, 863, 43
- Wolter, A., Consolandi, G., Longhetti, M., Landoni, M. & Bianco, A., in preparation
- Zezas, A., Fabbiano, G., Baldi, A., Schweizer, F., King, A. R., Rots, A. H. & Ponman, T. J., *ApJ*, 661, 135

Discussion

INDULEKHA KAVILA: You see misalignment between ULXs and the HII regions. Since there is a time gap between the star formation event and the appearance of the ULX, wouldn't it be more apt to look for alignment with signatures of B stars - which are the brightest objects in the "post star formation event" phase?

WOLTER: We have checked for offsets between the location of the peak of the optical emission and the ULX number density, with no particular selection of emission signatures.

CLAUS LEITHERER: One additional step would be to apply population synthesis models with binary star evolution (BPASS; Eldridge *et al.* 2017). This would allow you to model the optical and X-ray data simultaneously and check for consistency.

WOLTER: We thank you for the suggestion and we will try to implement this for the next publication.